Langmuir

Article

pubs.acs.org/Langmuir

Effect of Solvent Evaporation on Fiber Morphology in Rotary Jet Spinning

Holly McIlwee Golecki,[†,‡] Hongyan Yuan,[†,‡] Calla Glavin,[‡,§] Benjamin Potter,[‡,§] Mohammad R. Badrossamay,[‡] Josue A. Goss,[‡] Michael D. Phillips,[‡,§] and Kevin Kit Parker*[,‡,§]

[‡]Disease Biophysics Group, Wyss Institute for Biologically Inspired Engineering, School of Engineering and Applied Science, Harvard University, Cambridge, Massachusetts 02138, United States

[§]Department of Mathematical Sciences, United States Military Academy, West Point, New York 10996, United States

ABSTRACT: The bulk production of polymeric nanofibers is important for fabricating high-performance, nanoscale materials. Rotary jet spinning (RJS) enables the mass production of nanostructured fibers by centrifugal forces but may result in inconsistent surface morphologies. Because nanofiber performance is dependent upon its surface features, we asked which parameters must be optimized during production to control fiber morphology. We developed and tested a mathematical model that describes how the competition between fluid instability and solvent removal in RJS regulates the degree of beading in fibers. Our data suggest that solvent evaporation during the spinning process causes an increase in jet viscosity and that these changes inhibit both bead formation and jet thinning. The RJS was used to vary experimental parameters, showing that fiber beading can be reduced by increasing solvent volatility, solution viscosity, and spinning velocity. Collectively, our results demonstrate that nanofiber morphology and diameter can be precisely controlled during RJS manufacturing.

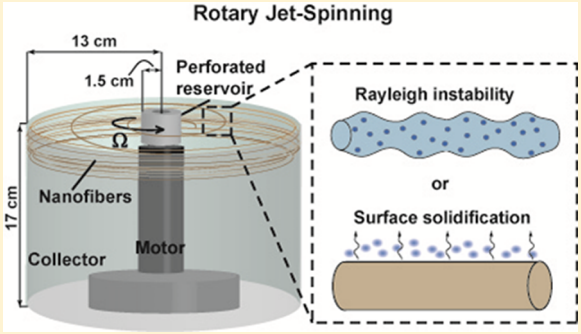

INTRODUCTION

Nanofibers are used for applications ranging from energy[1,2] to tissue engineering[3,4] because of their large surface area/volume ratio. For example, the energy-harvesting efficiency within nanofibers is proportional to its exposed surface area, which is maximized in fine, defect-free fibers.[2] Defects within a nanofiber-based scaffold for biological tissues may degrade cell migration and tissue genesis.[5−7] Although there has been significant effort to understand nanofiber geometry and surface topography through empirical studies[8−10] and modeling,[11−14] methods to control surface malformations or beading during bulk manufacturing remain elusive. To optimize nanomaterials for specialized applications, it is necessary to first identify and then control the parameter space used in fiber production.

Rotary jet spinning (RJS)[14−18] is an efficient and reproducible manufacturing technique developed for the bulk nanofiber production. In this system, a high-speed, rotating reservoir projects a fluid jet from a micrometer-sized orifice toward a collector. The high-speed rotation and solvent evaporation enables production of nanoscale polymer fibers. RJS surpasses the electrospinning technique[11,12,15] in both production rate and utility,[19] with speeds up to 5−6 times higher, while eliminating the requirements of an external electric field or a charged solution.[16] We asked how nanofiber morphology, including beading and fiber diameter, is regulated during RJS manufacturing. Previous analytical, empirical, and numerical studies suggest that fiber diameter is reduced by decreasing viscosity or increasing rotation speed.[13,14] However, decreasing either viscosity or rotation speed independently increases the incidence of surface defects, such as beading.[13]

We hypothesize that bead formation occurs because of Rayleigh instabilities within fluid jets and that smooth, bead-free fibers form as a result of faster solvent evaporation. We developed an analytical model that balances this fluid instability and fiber drying. To test the model, we manufactured fibers using solutions with a range of viscosities and solvent volatilities. Our results suggest a mechanism of bead reduction that depends upon not only tuning viscosity and rotation speed as formerly suggested[13] but also inhibition of Rayleigh instabilities via solvent evaporation.

MATERIALS AND METHODS

Solution Preparation. Polylactic acid (PLA, polymer 2002D, NatureWorks, Minnetonka, MN) was dissolved in chloroform (99.8%, Mallinckrodt Chemicals, Phillipsburg, NJ) and dimethylformamide (DMF, Sigma-Aldrich, St. Louis, MO) at room temperature by stirring.

Fiber Fabrication. The RJS system used to manufacture fibers is depicted in Figure 1a. The RJS consisted of a brushless DC servo motor (Maxon Motor Company, Fall River, MA) attached to a custom-fabricated reservoir with a 343 μm sidewall orifice. Solutions (1 mL) were spun at angular speeds, Ω, up to 75 000 rpm and collected at the spinning midpoint to ensure sample uniformity. Samples were Pt/Pd-coated using a sputter coater (Cressington

Received: June 16, 2014
Revised: October 9, 2014
Published: October 29, 2014

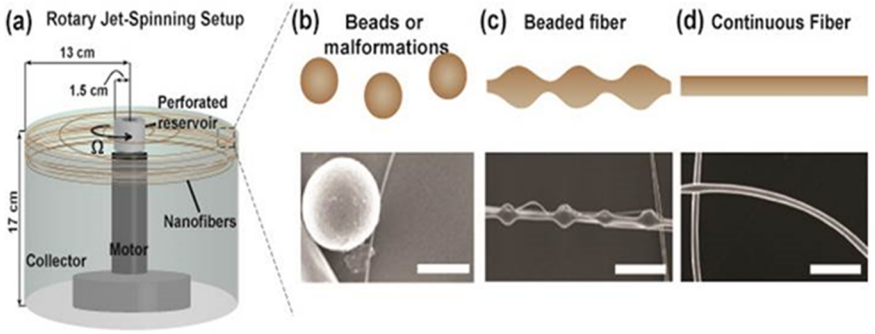

Figure 1. Variable fiber morphologies of RJS. (a) Schematic of the RJS setup. A solution of PLA (4 wt % in chloroform) is spun using RJS. Fibers collected have variable morphologies including (b) beads and malformations, (c) beads on a string (beaded fiber), or (d) continuous, defect-free fibers. (b–d) Scale bars are 20 μm.

208HR, Watford, U.K.) and imaged using Zeiss SUPRA field-emission scanning electron microscopy (SEM, Carl Zeiss, Dresden, Germany).

Solution Properties. Polymer solution surface tension was measured with a Sigma700 tensiometer (KSV Instruments, Espoo, Finland). Solution viscosity was measured in a rheometer (model AR-G2, TA Instruments, New Castle, DE) fitted with a standard-size recessed-end concentric cylinder geometry (model 988339, outer radius of 14 mm, inner radius of 15 mm, and 4000 μm gap) under a steady-state shear rate from 0.1 to 3000 s^{-1}.

Analysis. The number of beads or malformations in each experiment was calculated by manually thresholding SEM images in ImageJ (National Institute of Health, Bethesda, MD) and measuring polymer area in beads or malformations. Phase diagrams consist of points marking the transition from samples consisting of non-uniform fibers (samples with >5% beads or malformations) to samples consisting of continuous fibers (samples with <5% beads or malformations). A threshold value of 5% was chosen for consistency with previously published work.[13] A total of n = 24 fields of view at 2500× (~0.01 mm^2) and 7500× (~10^{-3} mm^2) magnification were analyzed per condition.

Flux of Mass Transfer of Solvent at the Jet Surface. The local steady-state convection–diffusion equation for the solvent mass concentration ρ near the jet surface can be approximated as $V_x(\partial\rho/\partial x) = D_{air}(\partial^2\rho/\partial y^2)$, where D_{air} is the solvent diffusion constant in air, the x axis is tangential to the local surface, the y axis is perpendicular to the local surface, and V_x is the air flow speed relative to the jet. A length scale of mass diffusion L_y near the local surface can be determined by scale analysis: $V_x(\rho/L_x) = D_{air}(\rho/L_y^2)$. Assuming $V_x \sim \Omega S_0$ and $L_x \sim R$, where R is the jet radius and S_0 is the reservoir radius, one has $L_y \sim (D_{air}R/\Omega S_0)^{1/2}$. The flux J for surface mass transfer can then be written as $J = D_{air}(\partial\rho/\partial y) \sim D_{air}(\rho_a/L_y)$, where ρ_a is the solvent vapor concentration in the air near the fiber surface. Substituting L_y into the flux equation $J \sim D_{air}(\rho_a/L_y)$ gives

$$J \sim \rho_a\left(\frac{D_{air}S_0}{R}\right)^{1/2}\Omega^{1/2} \tag{1}$$

Here, ρ_a can be related to solvent vapor pressure P by the ideal gas equation as $\rho_a = PM/R_{gas}T$, where M is the solvent molecule molar mass, R_{gas} is the ideal gas constant, and T is the temperature. When this expression of ρ_a is substituted into eq 1, solvent removal flux J can be approximated as

$$J \sim \frac{PM}{R_{gas}T}\left(\frac{D_{air}S_0}{R}\right)^{1/2}\Omega^{1/2} \tag{2}$$

Time Scale of Surface Layer Solidification. The time scale of surface layer solidification is much shorter than that of complete solvent evaporation. The surface layer solidification time scale is governed by two physical processes: (1) solvent evaporation at the boundary and (2) solvent diffusion from the fiber center to the boundary. The mass transport by diffusion in the long cylindrical jet can be treated as radially symmetric. Therefore, the solvent density ρ is a function of the radial coordinate r and time t only. The diffusion equation[20] can then be written as $\partial\rho/\partial t = (1/r)(\partial/\partial r)(rD(\partial\rho/\partial r))$, where $D \sim 10^{-7}$ cm^2/s is the solvent diffusion constant in the polymer solution.[21] The initial condition is $\rho(r,t = 0) = \rho_0$. The boundary conditions are $D(\partial\rho/\partial r)|_{r=R} = J$ and $\partial\rho/\partial r|_{r=0} = 0$, where ρ_0 is the initial solvent mass concentration in the jet and the flux J is given by eq 2. The solvent density at the jet surface ($r = R$) as a function of time can be written[20] as $\rho(R,t) = \rho_0 - (JR/D)\{(2Dt/(R^2)) + 1/4 - 2\sum_{n=1}^{\infty}((\exp(-D\alpha_n^2 t/R^2))/(\alpha_n^2))\}$, when $\alpha_n > 0$ and satisfies $J_1(\alpha_n) = 0$, where J_1 is the Bessel function of the first kind. Assuming that the solidification occurs at the surface when $\rho(R,t) = \bar{\rho}$, then the time scale τ_s can be obtained using the following equation:

$$\bar{\rho} = \rho_0 - \frac{JR}{D}\left\{\frac{2D\tau_s}{R^2} + \frac{1}{4} - 2\sum_{n=1}^{\infty}\frac{\exp\left(-\frac{D\alpha_n^2\tau_s}{R^2}\right)}{\alpha_n^2}\right\} \tag{3}$$

It can be numerically shown that the sum, $(2D\tau_s/(R^2)) + 1/4 - 2\sum_{n=1}^{\infty}((\exp(-D\alpha_n^2\tau_s/(R^2)))/(\alpha_n^2))$, is approximately equal to $(D\tau_s/(R^2))^{1/2}$ when $\tau_s \ll ((R^2)/D)$. The diffusion time scale, $((R^2)/D)$, is in the range from 10^{-1} to 10^{-3} s by estimating R from 10^{-7} to 10^{-6} m. For successful fiber formation, τ_s should be less than the spinning time scale, the reciprocal of angular spinning speed, which is ~10^{-3} s. Therefore, the condition $\tau_s \ll ((R^2)/D)$ is satisfied, and eq 3 can be simplified as $\bar{\rho} = \rho_0 - (JR/D)((D\tau_s/(R^2))^{1/2})$. When we solve for τ_s, we have $\tau_s = D(((\rho_0 - \bar{\rho})/J)^2)$. When eq 2 is substituted into it, we obtain the time scale of surface layer solidification as

$$\tau_s = \left(\frac{R_{gas}T}{PM}\right)^2\frac{DR(\rho_0 - \bar{\rho})^2}{D_{air}S_0\Omega} \tag{4}$$

Equation 4 is used to illustrate the effect of solvent evaporation on the fiber diameter and to derive the condition for production of continuous fibers.

RESULTS AND DISCUSSION

The RJS system consists of a rotating reservoir that extrudes a fluid jet from a micrometer-sized orifice toward a collector to form solid nanofibers (Figure 1a). To initiate fiber formation, polymer solutions are injected into the reservoir spinning at speeds, Ω, up to 75 000 rpm, projecting the jet through the 343 μm diameter orifice. The jet is elongated, traveling in a spiral trajectory toward a stationary cylindrical wall at ~10 cm from the reservoir. During this stage, polymer chains extend and entangle, while the solvent evaporates to yield a combination of malformed (Figure 1b), beaded (Figure 1c), and continuous (Figure 1d) nanofibers.

We first asked how the solvent evaporation rate of extruded polymer solutions impacts the final fiber diameter. The solvent removal process can be divided into two stages. In stage I, the

dx.doi.org/10.1021/la5023104 | Langmuir 2014, 30, 13369–13374

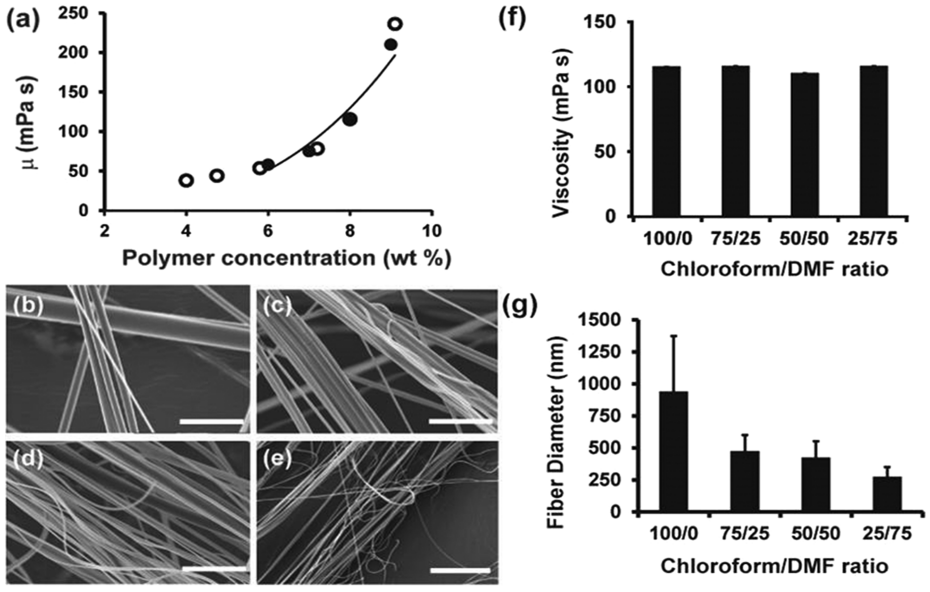

Figure 2. Effect of solvent volatility on fiber diameter. (a) Viscosity as a function of the polymer concentration for solutions of PLA in (○) 100:0 and (●) 75:25 chloroform/DMF. The line is fitted by a power law for $c \geq 6\%$ g/mL using chloroform and chloroform/DMF data points. SEM images of PLA fibers spun from a 8 wt % solution in (b) 100:0, (c) 75:25, (d) 50:50, and (e) 25:75 chloroform/DMF. (f) Viscosity of 8 wt % PLA solutions of 100:0, 75:25, 50:50, and 25:75 chloroform/DMF (n = 3 solutions measured per condition). (g) Graph of PLA nanofiber diameters with varying solvent conditions (n = 5 ROIs; 200 measurements per image). Error is standard deviation. (b–e) Scale bars are 5 μm.

jet travels in air, resulting in forced convective mass transfer of solvent at the jet surface. In this stage, the solvent evaporation rate is dependent upon the spinning speed. In stage II, the remaining solvent diffuses through the polymer matrix and evaporates after the fibers land on the collector. Because nanoscale fibers are collected immediately after spinning, we assume that fiber diameter is determined during jet elongation in stage I. Therefore, we focus on solvent evaporation in stage I. The solution viscosity remains nearly constant when the polymer concentration $c < 6\%$ g/mL, as shown in Figure 2a. Viscosity also increases with the polymer concentration by a power law ($\mu \sim \mu_i(c/c_i)^{3.2}$) when $c \geq 6\%$ g/mL, where $c_i \sim 6\%$ g/mL and $\mu_i \sim 58$ mPa s. Only a small amount of solvent evaporation is necessary in stage I to bring the polymer concentration at the jet surface to a viscosity high enough such that the polymer solution becomes solid-like. A previously obtained scaling relation between fiber radius R, viscosity μ, and angular spinning speed Ω[13] suggested that the fiber diameter increases with solution viscosity. However, the relationship between solvent evaporation and diameter has not been determined.

We hypothesize that faster solvent evaporation leads to increased jet viscosity and, hence, larger fiber diameters. To test this hypothesis empirically, we varied the ratios of chloroform and dimethylformamide (DMF) to tune the evaporation rate and measured fiber diameter using SEM and image analysis. Chloroform (vapor partial pressure P = 21.2 kPa) is a more volatile organic solvent than DMF (vapor partial pressure P = 0.36 kPa). Thus, increasing the ratio of chloroform/DMF increases the amount of solvent evaporation. Here, PLA nanofibers were formed from composite solutions containing chloroform/DMF ratios ranging from 100:0 to 25:75 (panels b–e of Figure 2). To determine the effect of solvent volatility on viscosity, we measured the viscosity for 8 wt % PLA solutions dissolved in chloroform/DMF ratios of 100:0, 75:25, 50:50, and 25:75. We observed no significant differences in viscosities as a function of solvent composition (Figure 2f). However, we found that fiber diameter increases with increasing solvent volatility (Figure 2g). These results suggest that a more volatile solvent leads to faster solvent evaporation, which increases the polymer concentration and viscosity during drying, resulting in larger fiber diameters. These results suggest that fiber diameter can vary independently of solution viscosity and rotation speed; specifically, increasing the solvent volatility leads to increased polymer concentration and, hence, fluid jet viscosity during stage I, resulting in larger diameter fibers.

To better illustrate the effect of solvent evaporation on fiber production, we derived a scaling relationship describing the time scale of jet surface solidification in stage I as a function of experimental parameters. In RJS, fibers move with a speed $\sim \Omega S_0$ relative to ambient air, where Ω is the angular spinning speed of the reservoir and $S_0 \sim 1.4$ cm is the radius of the reservoir. Solvent removal occurs by forced convective mass transfer at the jet surface. The Reynolds number Re of the air flow relative to fiber is $Re = (\Omega S_0 R/\nu_{air}) \sim 1$, where the kinematic viscosity of air at room temperature is $\nu_{air} \sim 1.6 \times 10^{-5}$ m^2/s. Assuming for low Reynolds numbers $Re \sim 1$, we derived the mass-transfer flux of solvent from the jet to air based on the convection–diffusion equation and the surface solidification time scale as $\tau_s = (R_{gas}T/PM)^2(DR((\rho_0 - \bar{\rho})^2)/D_{air}S_0\Omega)$ (which is eq 4 in the Materials and Methods). Equation 4 shows that higher volatility solvent results in larger fiber diameters as a consequence of jet surface solidification because of solvent evaporation slowing jet elongation. The theoretical result obtained here agrees qualitatively with the experimental data in Figure 2g, in which the fiber radius decreases as the solvent becomes less volatile.

Next, we asked if decreased solvent volatility decreased the number of surface defects. We sought to determine how the rate of solvent removal scaled with Rayleigh instability and subsequent bead formation using a theoretical approach. The Rayleigh instability theory states that cylindrical threads of

dx.doi.org/10.1021/la5023104 | Langmuir 2014, 30, 13369–13374

viscous fluid will develop instabilities or varicose morphology within a certain time scale.[22] This theory has been applied to polymer solutions in rheology,[23] threads of human saliva,[24] and electrospun jets[25] but has not been applied to RJS-formed fibers. In RJS, bead formation occurs because the surface tension is minimized in a spherical geometry, subsequently resulting in a minimized surface area. A simple geometric calculation shows that, when a long cylindrical jet breaks into spherical beads with a diameter larger than 1.5 times the initial jet diameter, the total surface area decreases. While surface tension drives bead formation, the surface solidification occurring in RJS inhibits beading when the jet becomes too viscous to flow into a varicose morphology, as depicted in Figure 3. A cylindrical polymer jet ejected from the RJS orifice

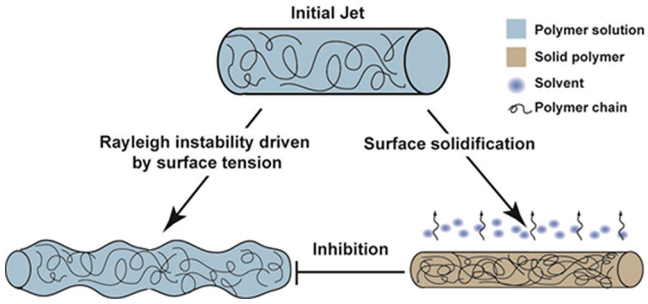

Figure 3. Schematic of forces acting on polymer solutions upon exiting the RJS orifice. Cylindrical polymer jets ejected from the spinning reservoir result in beaded or smooth fibers when the jet elongation stage is dominated by surface-tension-driven Rayleigh instabilities or solvent evaporation, respectively.

results in a smooth or beaded nanofiber. This result is potentiated by the competition between solvent removal and surface-tension-driven Rayleigh instabilities.

The time scale τ_b of beading for a cylindrical column of viscous fluid can be obtained by considering the force equilibrium between the viscosity $\mu(R/\tau_b/(R^2))$ and surface tension $\sigma/(R^2)$. Equating these two terms yields

$$\tau_b \sim \frac{R\mu}{\sigma} \tag{5}$$

The number of beads in RJS can be estimated by comparing the time scale of Rayleigh instability and that of surface solidification. Beaded fibers form when the time scale of Rayleigh instability, τ_b, is less than the time scale of surface solidification, τ_s. On the other hand, continuous fibers form when $\tau_b > \tau_s$, because the jet surface becomes solid-like before the fiber develops beads. When eqs 4 and 5 are substituted into the inequality $\tau_b > \tau_s$, we obtain the condition for the production of continuous fibers

$$\Omega\mu P^2 > C_{fit}\sigma\left(\frac{R_{gas}T}{M}\right)^2 \frac{D(\rho_0 - \bar{\rho})^2}{D_{air}S_0} \tag{6}$$

where C_{fit} is added as a numerical factor to be fitted. Equation 6 predicts that beading can be reduced by either decreasing the rate of Rayleigh instability (e.g., increasing viscosity μ), or increasing the rate of surface solidification.

To test whether our model can predict bead formation, we used the RJS to spin fibers from varying solutions of PLA dissolved in chloroform and chloroform/DMF (75:25) solvents (Figure 4). The resulting fiber morphologies were analyzed within a phase diagram in the $\Omega-\mu$ space, as shown in Figure 4. The circles mark the transition from continuous fibers with less than 5% beads to beaded fibers for PLA spun in chloroform/DMF (75:25) (Figure 4a). For example, fibers spun at 35 000 rpm from 7.5% PLA in chloroform/DMF (75:25) have <5% beads (Figure 4b). However, samples spun at low viscosity and moderate speed (2.5 wt % at 25 000 rpm; Figure 4c) or high viscosity and low speed (7.5 wt % at 10 000 rpm; Figure 4d) have significantly more beading present. The curve in Figure 4a marks the transition boundaries from the model predictions, plotting $\Omega = (1/(P^2))C_{fit}\sigma((R_{gas}T/M)^2)(D((\rho_0 - \bar{\rho})^2)/D_{air}S_0)\text{-}\mu^{-1}$. In Figure 4a, region I above the transition curve indicates the continuous-fiber phase (Figure 4b), while the regions below the transition curves are the beaded phase (panels c and d of Figure 4). The trend of the experimentally determined transition boundaries (○ in Figure 4a and ● in Figure 4e) match with the model predictions (- - - in Figure 4a and — in Figure 4e) that show increasing Ω or μ reduces beading.

To further demonstrate the utility of our model for multiple solvent volatilities, we compared it to an empirical phase diagram for PLA in chloroform only. We show that our model similarly matches our experimental data (Figure 4e) repeated

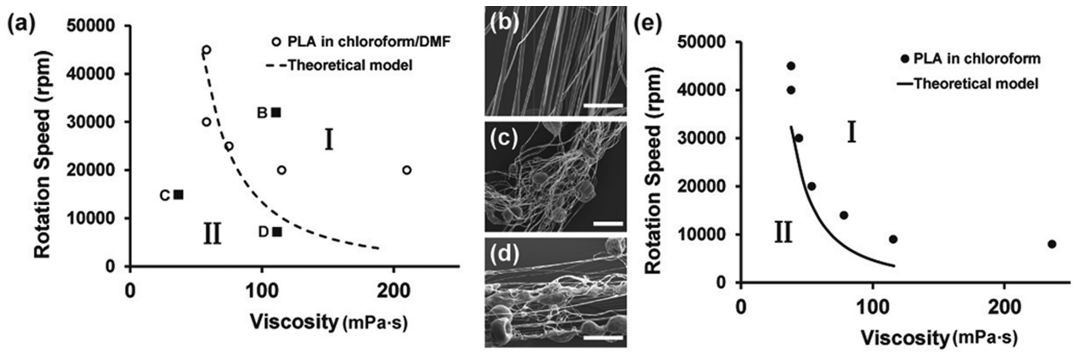

Figure 4. (a) Phase diagram of PLA nanofibers spun in chloroform/DMF (75:25) is plotted in the angular speed (Ω)−solution viscosity (μ) plane. (○) Experimentally determined transition between fibers with <5% beads (regime I) and >5% beads (regime II). (b) Fibers spun at 35 000 rpm from 7.5% PLA in chloroform/DMF (75:25). (c) Fibers spun at 25 000 rpm from 2.5% PLA in chloroform/DMF (75:25). (d) Fibers spun at 10 000 rpm from 7.5% PLA in chloroform/DMF (75:25). (e) Phase diagram of PLA nanofibers spun in chloroform is plotted in the $\Omega-\mu$ plane. (●) Transition from <5% beads (regime I) to >5% beads (regime II). Equation 6 is plotted for both panels a and e and qualitatively agrees with the experimental data.

dx.doi.org/10.1021/la5023104 | Langmuir 2014, 30, 13369−13374

from empirical phase diagrams previously published.[13] In addition, eq 6 predicts that, when the solvent volatility P increases, the transition curve will move downward in the $\Omega-\mu$ space. This is suggested by comparing the experimental data in Figure 4a to those in Figure 4e, suggesting that the beading transition curve shifts downward as the solvent becomes less volatile [chloroform in Figure 4e compared to chloroform/DMF (75:25) in Figure 4a]. Additionally, these data suggest that lower spinning speeds are required to form continuous fibers using highly volatile solvents and other common solutions, including less volatile, aqueous solvents, would require higher spinning speeds to form defect-free fibers. In other words, more volatile solvents increase the range of the continuous-fiber phase in the $\Omega-\mu$ space, meaning a broader range of fiber diameters can be obtained. This addition enables the production of continuous fibers and less beaded structures during nanofiber production.

CONCLUSION

From our results, we conclude that the physical mechanism of bead formation in RJS is a competition between the time scales of Rayleigh instability and solvent evaporation rate. Our experimental data and theoretical analysis reveal that fiber drying, a result of solvent evaporation, plays an important role in determining nanofiber morphology in RJS. The solvent evaporation rate can be controlled by changing solvent volatility and rotation speed. Increasing solvent volatility while holding viscosity constant produces larger fiber diameters by inhibiting jet thinning. However, increasing both solvent volatility and spinning speed prohibits bead formation in RJS fibers by increasing the polymer concentration in the jet and drying fibers before Rayleigh instabilities develop. The analytical model that we derived here can be used for precise morphology control during production. These findings may increase the utility of RJS when forming nanoscale materials with applications that require defect-free fibers, such as energy harvesting and tissue engineering.

AUTHOR INFORMATION

Corresponding Author

*Telephone: 617-495-2850. Fax: 617-495-9837. E-mail: kkparker@seas.harvard.edu.

Author Contributions

†Holly McIlwee Golecki and Hongyan Yuan contributed equally to this work.

Notes

The authors declare no competing financial interest.

ACKNOWLEDGMENTS

The authors acknowledge L. Mahadevan for helpful discussions. The authors thank Leila F. Deravi and Alexander P. Nesmith for reviewing the manuscript. The authors acknowledge financial support of this work from Wyss Institute for Biologically Inspired Engineering, Harvard University Materials Research Science and Engineering Center (MRSEC), Harvard University Nanoscale Science and Engineering Center (NSEC), and Harvard Center for Nanoscale Systems (CNS). Holly McIlwee Golecki acknowledges the National Science Foundation Graduate Research Fellowship Program.

REFERENCES

(1) Persano, L.; Dagdeviren, C.; Su, Y.; Zhang, Y.; Girardo, S.; Pisignano, D.; Huang, Y.; Rogers, J. A. High performance piezoelectric devices based on aligned arrays of nanofibers of poly(vinylidenefluoride-*co*-trifluoroethylene). *Nat. Commun.* **2013**, *4*, 1633.

(2) Thavasi, V.; Singh, G.; Ramakrishna, S. Electrospun nanofibers in energy and environmental applications. *Energy Environ. Sci.* **2008**, *1* (2), 205−221.

(3) Lutolf, M. P.; Hubbell, J. A. Synthetic biomaterials as instructive extracellular microenvironments for morphogenesis in tissue engineering. *Nat. Biotechnol.* **2005**, *23* (1), 47−55.

(4) Pham, Q. P.; Sharma, U.; Mikos, A. G. Electrospinning of polymeric nanofibers for tissue engineering applications: A review. *Tissue Eng.* **2006**, *12* (5), 1197−1211.

(5) Lutolf, M. P.; Gilbert, P. M.; Blau, H. M. Designing materials to direct stem-cell fate. *Nature* **2009**, *462* (7272), 433−441.

(6) Stevens, M. M.; George, J. H. Exploring and engineering the cell surface interface. *Science* **2005**, *310* (5751), 1135−1138.

(7) Ruder, W. C.; Pratt, E. D.; Bakhru, S.; Sitti, M.; Zappe, S.; Cheng, C.; Antaki, J. F.; LeDuc, P. R. Three-dimensional microfiber devices that mimic physiological environments to probe cell mechanics and signaling. *Lab Chip* **2012**, *12*, 1775−1779.

(8) Bhattacharjee, P. K.; Schneider, T. M.; Brenner, M. P.; McKinley, G. H.; Rutledge, G. C. On the measured current in electrospinning. *J. Appl. Phys.* **2010**, *107* (4), No. 044306.

(9) Gu, S. Y.; Ren, J. Process optimization and empirical modeling for electrospun poly(D,L-lactide) fibers using response surface methodology. *Macromol. Mater. Eng.* **2005**, *290* (11), 1097−1105.

(10) Thompson, C. J.; Chase, G. G.; Yarin, A. L.; Reneker, D. H. Effects of parameters on nanofiber diameter determined from electrospinning model. *Polymer* **2007**, *48* (23), 6913−6922.

(11) Feng, J. J. The stretching of an electrified non-Newtonian jet: A model for electrospinning. *Phys. Fluids* **2002**, *14* (11), 3912−3926.

(12) Fridrikh, S. V.; Yu, J. H.; Brenner, M. P.; Rutledge, G. C. Controlling the fiber diameter during electrospinning. *Phys. Rev. Lett.* **2003**, *90* (14), No. 144502.

(13) Mellado, P.; McIlwee, H. A.; Badrossamay, M. R.; Goss, J. A.; Mahadevan, L.; Parker, K. K. A simple model for nanofiber formation by rotary jet-spinning. *Appl. Phys. Lett.* **2011**, *99*, No. 203107.

(14) Padron, S.; Fuentes, A.; Caruntu, D.; Lozano, K. Experimental study of nanofiber production through forcespinning. *J. Appl. Phys.* **2013**, *113* (2), No. 024318.

(15) Badrossamay, M. R.; McIlwee, H. A.; Goss, J. A.; Parker, K. K. Nanofiber assembly by rotary jet-spinning. *Nano Lett.* **2010**, *10* (6), 2257−2261.

(16) Huttunen, M.; Kellomaki, M. A simple and high production rate manufacturing method for submicron polymer fibres. *J. Tissue Eng. Regener. Med.* **2011**, *5* (8), E239−E243.

(17) Nayak, R.; Padhye, R.; Kyratzis, I.; Truong, Y. B.; Arnold, L. Recent advances in nanofibre fabrication techniques. *Text. Res. J.* **2012**, *82* (2), 129−147.

(18) Sarkar, K.; Gomez, C.; Zambrano, S.; Ramirez, M.; de Hoyos, E.; Vasquez, H.; Lozano, K. Electrospinning to Forcespinning™. *Mater. Today* **2010**, *13* (11), 12−14.

(19) Senthilram, T.; Mary, L. A.; Venugopal, J. R.; Nagarajan, L.; Ramakrishna, S.; Dev, V. R. G. Self crimped and aligned fibers. *Mater. Today* **2011**, *14* (5), 226−229.

(20) Crank, J. *The Mathematics of Diffusion*, 2nd ed.; Oxford University Press: Oxford, U.K., 1975.

(21) Perioto, F. R.; Alvarez, M. E. T.; Araujo, W. A.; Wolf-Maciel, M. R.; Maciel Filho, R. Development of a predictive model for polymer/solvent diffusion coefficient calculations. *J. Appl. Polym. Sci.* **2008**, *110* (6), 3544−3551.

(22) Lee, W. K.; Flumerfelt, R. W. Instability of stationary and uniformly moving cylindrical fluid bodies. 1. Newtonian systems. *Int. J. Multiphase Flow* **1981**, *7* (4), 363−383.

(23) Oliveira, M. S. N.; Yeh, R.; McKinley, G. H. Iterated stretching, extensional rheology and formation of beads-on-a-string structures in

polymer solutions. *J. Non-Newtonian Fluid Mech.* **2006**, *137* (1-3), 137−148.
(24) Sattler, R.; Gier, S.; Eggers, J.; Wagner, C. The final stages of capillary break-up of polymer solutions. *Phys. Fluids* **2012**, *24* (2), No. 023101.
(25) Yu, J. H.; Fridrikh, S. V.; Rutledge, G. C. The role of elasticity in the formation of electrospun fibers. *Polymer* **2006**, *47* (13), 4789−4797.